Journal of Hazardous Materials 467 (2024) 133753

Contents lists available at ScienceDirect

Journal of Hazardous Materials

journal homepage: www.elsevier.com/locate/jhazmat

Heteroatom substitution enhances generation and reactivity of surface-activated peroxydisulfate complexes for catalytic fenton-like reactions

Yan Wei [a], Jie Miao [a], Jiahao Cui [a], Junyu Lang [b], Qunli Rao [c], Baoxue Zhou [a], Mingce Long [a,*], Pedro J.J. Alvarez [d,*]

[a] School of Environmental Science and Engineering, Shanghai Jiao Tong University, Shanghai 200240, China
[b] School of Physical Science and Technology, ShanghaiTech University, Shanghai 201210, China
[c] Instrumental Analysis Center, Shanghai Jiao Tong University, Shanghai 200240, China
[d] Department of Civil and Environmental Engineering, Rice University, Houston, TX 77005, United States

HIGHLIGHTS

- Zn incorporated into CuO lattice and optimized electronic structure of Cu sites.
- PDS oxidation performance was improved by enhancing PDS* generation and reactivity.
- Zn substitution enhanced PDS* generation by promoting PDS adsorption.

GRAPHICAL ABSTRACT

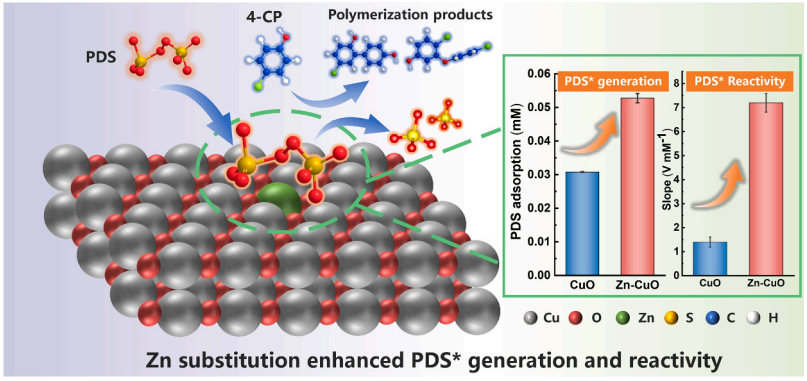

ARTICLE INFO

Keywords:
Persulfate activation
Heteroatom substitution
PDS adsorption
Surface-activated complexes

ABSTRACT

Peroxydisulfate (PDS)-based Fenton-like reactions are promising advanced oxidation processes (AOPs) to degrade recalcitrant organic water pollutants. Current research predominantly focuses on augmenting the generation of reactive species (e.g., surface-activated PDS complexes (PDS*) to improve treatment efficiency, but overlooks the potential benefits of enhancing the reactivity of these species. Here, we enhanced PDS* generation and reactivity by incorporating Zn into CuO catalyst lattice, which resulted in 99% degradation of 4-chlorophenol within only 10 min. Zn increased PDS* generation by nearly doubling PDS adsorption while maintaining similar PDS to PDS* conversion efficiency, and induced higher PDS* reactivity than the common catalyst CuO, as indicated by a 4.1-fold larger slope between adsorbed PDS and open circuit potential of a catalytic electrode. Cu-O-Zn formation upshifts the d-band center of Cu sites and lowers the energy barrier for PDS adsorption and sulfate desorption, resulting in enhanced PDS* generation and reactivity. Overall, this study informs strategies to enhance PDS* reactivity and design highly active catalysts for efficient AOPs.

* Corresponding authors.
E-mail addresses: long_mc@sjtu.edu.cn (M. Long), alvarez@rice.edu (P.J.J. Alvarez).

https://doi.org/10.1016/j.jhazmat.2024.133753
Received 14 December 2023; Received in revised form 23 January 2024; Accepted 6 February 2024
Available online 9 February 2024

1. Introduction

The discharge of persistent and toxic organic contaminants into aquatic ecosystems poses a significant challenge to environmental health and clean water supply [1,6,34]. Heterogenous persulfate-based Fenton-like reactions utilizing peroxymonosulfate (PMS, HSO_5^-) and peroxodisulfate (PDS, $S_2O_8^{2-}$) are promising water treatment technologies to remove recalcitrant organic contaminants, due to their high efficiency and affordability [11,27,41]. Compared to PDS salts (e.g., $K_2S_2O_8$), commercial PMS (i.e., Oxone) is more costly ($ 0.74/kg vs. $ 2.2/kg) and contains $KHSO_4$ and K_2SO_4 impurities, which decreases the pH and reduces the effective oxidant mass content [25,46,48]. Moreover, PMS possesses more susceptible asymmetric O-O bonds, thus being more inclined to be activated via interferential hybrid pathways and lower oxidant utilization efficiency [31]. Despite these advantages, current cutting-edge research on persulfate-based AOPs predominantly focuses on PMS-based systems, because of steric hindrance caused by the presence of two SO_3 moieties on both sides of an O–O bond, making PDS less reactive than PMS [16]. Thus, it is important to overcome these limitations and develop efficient PDS-based oxidation systems that enhance the feasibility of persulfate-based AOPs in wastewater treatment.

Typically, PDS activation is initiated by its adsorption onto active sites to generate radical (e.g., $SO_4^{\bullet-}$ and $^{\bullet}OH$) [8,63] or nonradical reactive species (e.g.,$^1O_2$, high-valent metals, and surface-activated PDS complexes (PDS*) [24,40,49] that oxidize the target pollutants. Thus, the overall efficiency of these AOPs depends on two factors: (1) the generation of reactive species, which hinges on the adsorption of persulfate and the conversion of the adsorbed persulfate into reactive species, and (2) the reactivity of these species, which is related on their oxidation capacity and the electron transfer rate with pollutants. Among the generated reactive species, PDS* are commonly formed over the surface of catalysts such as carbon materials [15,38] and metal oxides [44,57]. These complexes exhibit high selectivity toward electron-rich pollutants [12,53], stability in water matrices [10,47], and propensity to avoid the formation of toxic halogenated byproducts [7,54]. They also exhibit surface-confined metastable states, hinting at the potential for tunable generation and reactivity through manipulation of the catalyst structure and composition [16,31]. For example, heteroatom substitution engineering, which modifies the electronic structure of active sites, can optimize both the adsorption and activation of persulfate [39,49,50,55,9]. The incorporation of adjacent Cu atoms into a carbon-supported single Cu atom catalyst was reported to facilitate PDS adsorption, leading to the formation of PDS complexes (PDS*) through a dual-site mode [43]. N doping was shown to facilitate the generation of peroxymonosulfate complexes (N-CNT-PMS*), thus further boosting phenol degradation [32] Similarly, the introduction of cobalt (Co) into carbon nanotubes (Co-N-CNT) resulted in a high spin state of Co-N moieties, thus enhancing the PMS complexes generation [26]. While these efforts are promising to enhance the generation of such reactive complexes, strategies to enhance their reactivity remain largely unexplored, which represents an overlooked opportunity to inform the design of highly active catalysts for Fenton-like-based wastewater treatment.

Copper oxide (CuO), known for its low cost, facile synthesis and structural tunability, is a common catalyst for PDS activation via the PDS* pathway [23,29,57]. In this work, a Zn-doped CuO catalyst (Zn-CuO) was developed by substituting Cu with Zn heteroatoms, to explore the simultaneous regulation of PDS* generation and reactivity. Zn impurities were chosen because: (1) incorporation of non-metal sites such as B [28,61], N [50], and S [3,65] atoms into metal oxide substrates encounters susceptibility to replacement by O atoms, which requires intricate synthesis procedures and often results in unsatisfactory stability [2]; and (2) in contrast to conventional metal heteroatoms such as Mn [21], Co [62,63], and Au [51] substitution that create new active sites, earth-abundant Zn^{2+} with a fully occupied electronic configuration ($3d^{10}$) is inert and can replace Cu^{2+} without creating oxygen vacancies [22,35,5,56]. Remarkably, Zn substitution resulted in significantly improved PDS activation for 4-chlorophenol (4-CP) degradation via surface-activated Zn-CuO/PDS complexes (Zn-CuO/PDS*). The mechanism of Zn substitution for the enhancement of both PDS* generation and PDS* reactivity was discerned through both experimental and theoretical investigations.

2. Material and methods

2.1. Chemicals and materials

Details of chemicals and materials are listed in **Text S1**.

2.2. Catalyst preparation and characterization

Zinc-substituted copper oxide was synthesized using a modified precipitation method [45]. Briefly, a mixture containing $Cu(NO_3)_2$ and $Zn(NO_3)_2$ was alkalized by the gradual addition of NaOH (4 M). After aging at 90 ℃ for 2 h, catalysts with different Zn contents were prepared (labeled as Zn-CuO-*x*, where *x*% represented the theoretical mass ratio of Zn to CuO). If not specified, Zn-CuO-5 is simplified as Zn-CuO.

The crystalline phase of the catalyst was analyzed using X-ray diffraction (XRD, D8 Advance Da Vinci, Bruker) with Cu Kα radiation (λ = 0.154 nm). Rietveld refinement was conducted by the General Structure Analysis System (GSAS) software. X-ray photoelectron spectroscopy (XPS) analysis was gained by an AXIS Ultra DLD system (Shimadzu). The X-ray absorption spectroscopy (XAS) measurements were conducted at the BL14W beamline of the Shanghai Synchrotron Radiation Facility. Transmission electron microscopy (TEM, Talos F200X, FEI) images were recorded to observe the morphologies of Zn-CuO. The Brunauer-Emmett-Teller (BET) specific surface area was measured using a gas sorption analyzer (Autosorb-IQ3, Quantachrome). In situ Raman spectra at 532 nm were acquired by a Bruker Senterra R200-L dispersive Raman microscope. The occurrence of reactive oxygen species (ROS) was examined by a Bruker micro EPR spectrometer.

2.3. Catalytic activity evaluation

Batch degradation experiments were carried out by dispersing Zn-CuO (0.2 g/L) into 50 mL of 4-CP solution (10 mg/L) with stirring to achieve adsorption equilibrium. Then the reaction was initiated by adding PDS (0.2 mM) with an initial pH of 7.0. The sample (0.5 mL) was withdrawn and filtered at each predetermined time interval.

2.4. Analytical methods

The concentrations of 4-CP and its degradation byproducts were quantified by high-performance liquid chromatography (HPLC) on a Shimadzu LC-2010AHT instrument. The residual PDS concentration was measured through a KI spectrophotometry method [20,58]. To determine the oxidation potential of the generated surface complexes (PDS*), open-circuit potential measurement was performed in a three-electrode cell connected to an electrochemical workstation (CHI 760) by using catalyst-modified carbon paper as the working electrode with the addition of certain doses of PDS. The counter electrode and reference electrode are Pt wire and a saturated calomel electrode, respectively. Details of analytical methods are listed in **Text S2**.

Each test, performed in triplicate, is presented as mean values with error bars depicting ± one standard deviation. Statistical analysis involved a single-tailed Student's paired t-test with a significance $< 5\%$.

2.5. Theoretical calculations

All spin-polarized periodic calculations were carried out using the Vienna ab initio Simulation Package (VASP). Details of theoretical calculations are provided in **Text S3**.

3. Results and discussion

3.1. Zn-doped CuO catalyst exhibits heteroatom substitution of Cu by Zn

The synthesis procedure of Zn-substituted CuO (Zn-CuO) is illustrated in Fig. S1. The Zn content in Zn-CuO was 2.5 ± 0.007 wt%, based on inductively coupled plasma-atomic emission spectrometry (ICP-AES) (Table S1). The TEM image (Fig. 1a) reveals a stacked nanosheet structure of Zn-CuO, similar to pure CuO (Fig. S2). Zn modification did not significantly affect the BET specific surface area (Fig. S3). High-resolution transmission electron microscopy (HRTEM) and selected area electron diffraction (SAED) patterns show a lattice fringe spacing of 0.25 nm, corresponding to the CuO (−111) facet (inset in Fig. 1a). The elemental mapping image (Fig. 1b) corroborates that Zn was uniformly distributed over Zn-CuO.

No impurity phase of Zn was observed in the monoclinic phase of CuO (JCPDS No. 45–0937) even with a relatively high mass ratio (10%) of Zn precursors (Fig. S4). Rietveld-refined XRD patterns show that Zn-CuO maintains the same crystal structures as CuO, with a space group of *C1c1* (Fig. 1c and Table S2). It suggests that Zn atoms successfully incorporate into the CuO lattice through Cu substitution, facilitated by the similar ion radius of Cu^{2+} (R_{Cu2+} = 0.57 Å) and Zn^{2+} (R_{Zn2+} = 0.60 Å) [37]. Such substitution leads to increased unit cell volume and changed constants (*a*, *b*, and *c*) of Zn-CuO compared to pristine CuO, suggesting the lattice distortion (Table S2). Noticeable redshifts in Raman peaks were also observed with the increase in Zn content (Fig. S5). This suggests elongation of the Cu-O bond due to Zn substitution, which aligns with the expansion of Zn-CuO unit cells [50,52].

The surface chemical composition of catalysts was investigated using XPS. The XPS fitting curves of Cu 2p and Zn 2p demonstrate that both Cu and Zn exhibit an oxidation state of +2 in all tested samples (Fig. S6) [42]. Cu LMM spectra, which are particularly sensitive to the oxidation states of Cu, reveal that the ratio of the lower valent Cu ($Cu^{+2-\delta}$) is subsequently increased with the higher degree of Zn substitution (Fig. 1d), accompanied by an increasing Zn^{2+} ratio in Zn LMM peaks (Fig. S7) [13]. The lower Cu oxidation states observed after Zn substitution suggest an increase in electron density on the Cu atoms, which can be attributed to the higher electronegativity of Cu than that of Zn (χ_{Cu} = 1.90, χ_{Zn} = 1.65) [30,37].

The chemical state and coordination environment of Cu sites were analyzed by X-ray absorption fine structure spectroscopy (XAFS) measurements. The normalized X-ray absorption near-edge structure (XANES) spectra (Fig. 1**e**) demonstrate the absorption intensity for Zn-CuO is close to that of CuO, indicating a Cu oxidation state of approximately +2. However, Zn substitution resulted in a shift of the Cu K absorption edge toward lower energy, suggesting a decreased oxidation state of Cu sites, which is consistent with the XPS analysis. The presence of lower-valence Cu atoms in Zn-CuO is beneficial for electron transfer from Cu atoms to adsorbed PDS molecules [42]. Extended X-ray absorption fine structure spectra (EXAFS) in Fig. 1f reveal a dominant peak at 1.50 Å in both Zn-CuO and CuO, corresponding to the first shell Cu–O coordination [50]. The fitted coordination number (4.0) of Cu atoms remained unchanged after Zn substitution, indicating no generation of oxygen vacancies (Fig. S8 and Table S3) [36]. The absence of oxygen vacancies was further supported by the unobservable signals in the electron paramagnetic resonance (EPR) measurements (Fig. S9). The Cu–O–Cu peak, initially at 2.49 Å in CuO, shifts to 2.53 Å after Zn atom introduction, providing evidence for the presence of Cu–O–Zn second shell coordination [14].

3.2. Zn substitution enhanced catalytic performance in Fenton-like reactions

The Fenton-like reaction activity of Zn-CuO-*x* catalysts was assessed by oxidative 4-CP degradation through PDS activation. A “volcano-like” relationship between Zn contents and the first-order rate constants (k_{obs})

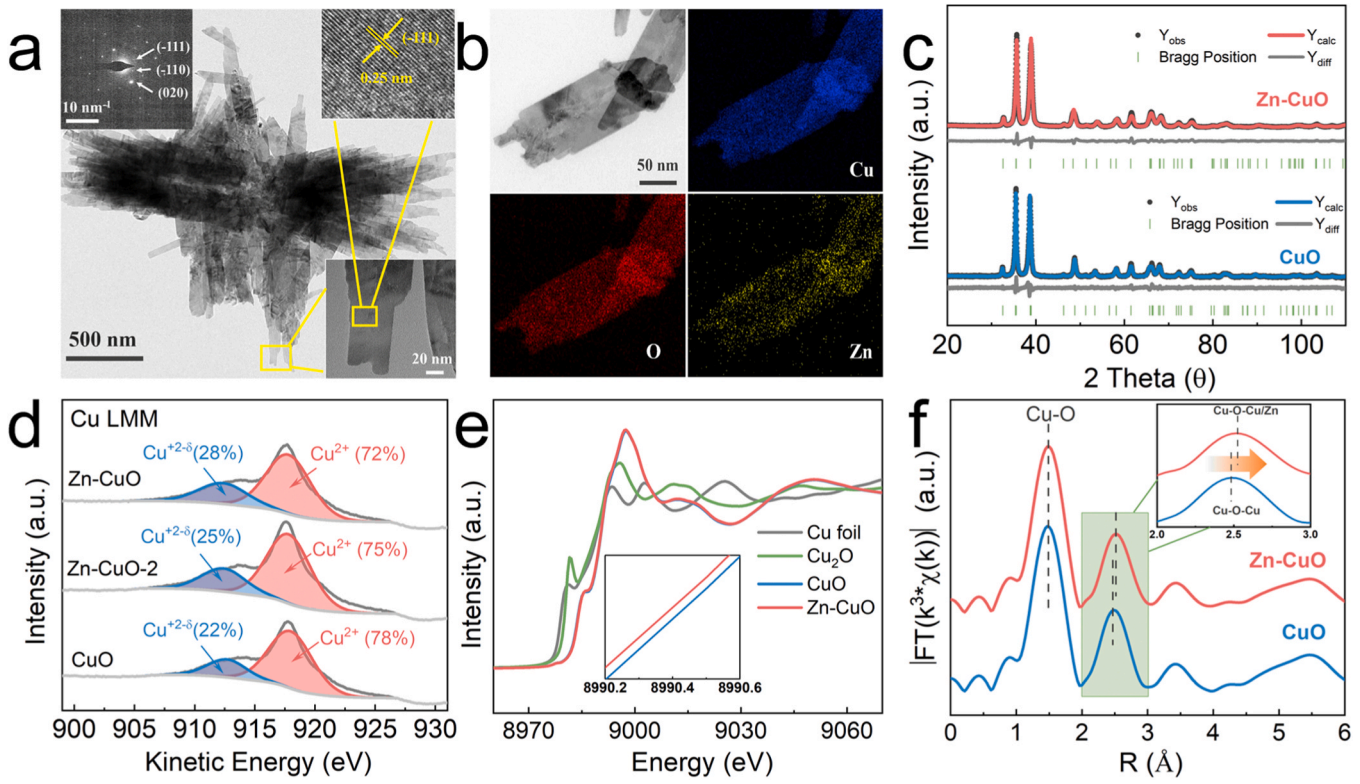

Fig. 1. (a) TEM image of Zn-CuO (insets are SAED and HRTEM images); (b) Elemental mapping images of Zn-CuO; (c) Rietveld-refined XRD patterns of CuO and Zn-CuO; (d) Cu LMM XPS spectra of prepared catalysts; (e) Normalized Cu K-edge XANES spectra of Zn-CuO and reference samples (Cu foil, Cu_2O, and CuO), and (f) Fourier transform k^3-weighted EXAFS spectra of CuO and Zn-CuO.

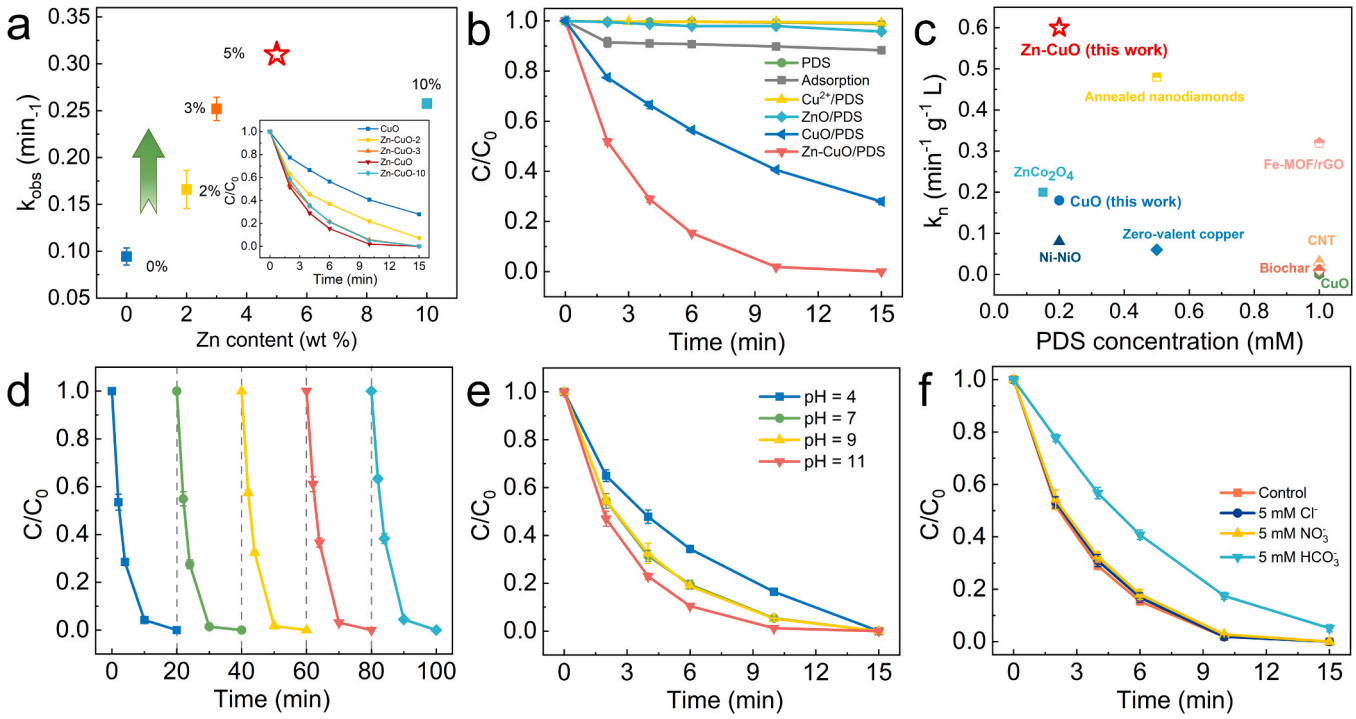

Fig. 2. (a) 4-CP degradation and first-order rate constants for Zn-CuO-*x* activated PDS; (b) 4-CP degradation under different conditions; (c) A comparison of 4-CP removal performance (by normalized rate constant *kn*) in different PDS systems; (d) Sustained 4-CP degradation activity by the Zn-CuO/PDS system in repeated batch reactions; (e) Influence of initial pH and (f) coexisting anions on 4-CP degradation in the Zn-CuO/PDS system. Conditions: $[4\text{-CP}]_0$ = 10 mg/L, [catalyst] = 0.2 g/L, $[Cu^{2+}]$ = 0.16 g/L, [PDS] = 0.2 mM, initial pH = 7.0.

of 4-CP degradation was observed (Fig. 2a), with a peak of 0.31 min^{-1} corresponding to 5 wt% Zn. Control tests (Fig. 2b) show that 12% of 4-CP was adsorbed and only 2% was directly oxidized by PDS within 15 min. Cu^{2+} or ZnO addition in the presence of PDS resulted in minimal 4-CP degradation. CuO exhibited limited PDS activation performance, leading to 78% 4-CP removal within 15 min (k_{obs} = 0.09 min^{-1}). In contrast, Zn-CuO addition with only 0.2 mM PDS achieved 99% degradation of 4-CP within 10 min, indicating the superior performance of Zn-CuO for efficient PDS utilization and activation. This resulted in an exceptionally high normalized rate constant (k_n) of 0.60 min^{-1} g^{-1} L, surpassing the values observed for other metal-based catalysts with similar surface areas and carbon-based catalysts known for their relatively high surface areas (Fig. 2c and Table S4) [18].

Zn-CuO demonstrated remarkable stability, as evidenced by maintaining almost 100% 4-CP degradation within 10 min over five cycles (Fig. 2d). No noticeable change in crystalline structure (Fig. S10) was observed after repeated reactions. Zn-CuO also exhibited high catalytic performance in complex environments, including stability across a wide pH range of 4 - 11 and resistance to various co-occurring constituents (Fig. 2e-f), suggesting it is promising for practical wastewater treatment. The intermediates formed during 4-CP degradation were further determined by ultra-performance liquid chromatography-mass spectrometry (UPLC-MS). Products resulting from C–C coupling and C–O polymerization were observed, with the polymerization degree even reaching 4 (Fig. S11). Such polymerized products could be easily separated by filtration and removed from water as part of the treatment process.

3.3. *Surface-activated PDS complexes-dominated Fenton-like reaction*

Quenching and EPR tests were performed to identify the primary reactive species responsible for 4-CP degradation. The presence of methanol (MeOH) and sodium fluoride (NaF) had a negligible impact on 4-CP degradation, indicating a minimal contribution from both free and surface-bound hydroxyl and sulfate radicals (Fig. 3a) [19]. The absence of detectable DMPO-$^{\bullet}$OH and DMPO-$SO_4^{\bullet-}$ signals in EPR tests further supported the nonradical activation pathway (Fig. S12a). Similarly, the involvement of $^1O_2$ in 4-CP removal was ruled out due to the limited inhibition of FFA on 4-CP degradation and the absence of TEMP-$^1O_2$ signals (Fig. S12b). The presence of 4-CP accelerated PDS decomposition from 21% to 40% within 15 min (Fig. 3b). This trend differs from the behavior observed in the Cu(III)-dominated CuO/PMS system, where Cu (III) preferentially reacts with 4-CP, leading to a slower consumption of the oxidant after 4-CP addition [45].

In situ Raman tests were conducted to identify the formation of PDS*. No significant peak was observed at 608 cm^{-1} throughout the reaction (Fig. 3c), suggesting the absence of Cu(III) during 4-CP degradation [4]. The characteristic peak of $S_2O_8^{2-}$ was detected at approximately 835 cm^{-1}. Following the introduction of Zn-CuO, a new peak emerged at around 816 cm^{-1}, corresponding to the bending vibrations of the prolonged O–O bond in the Zn-CuO/PDS* intermediate [33,59]. This peak gradually diminished upon the addition of 4-CP, highlighting the crucial role of the generated surface-activated Zn-CuO/PDS* in the degradation of 4-CP. The presence of surface-activated PDS* was also evident through the analysis of open-circuit potentials (Fig. 3d). Upon the addition of PDS, the open-circuit potential immediately increased and eventually reached an equilibrium state, indicating the generation of oxidative PDS*. Subsequently, as 4-CP was introduced, the potential decreased, which can be attributed to PDS* consumption during 4-CP degradation. A high ion concentration ([$NaClO_4$]: [PDS] = 50:1) did not significantly inhibit 4-CP degradation, suggesting inner-sphere complexation between Zn-CuO and PDS (Fig. S13) [9]. Therefore, the 4-CP degradation in Zn-CuO/PDS can be ascribed to the surface-activated PDS* pathway (Fig. S14). A similar pathway was also evidenced in the CuO/PDS system (Fig. S15), suggesting the improved PDS activation performance after Zn substitution is not attributed to the alteration of the PDS activation pathway.

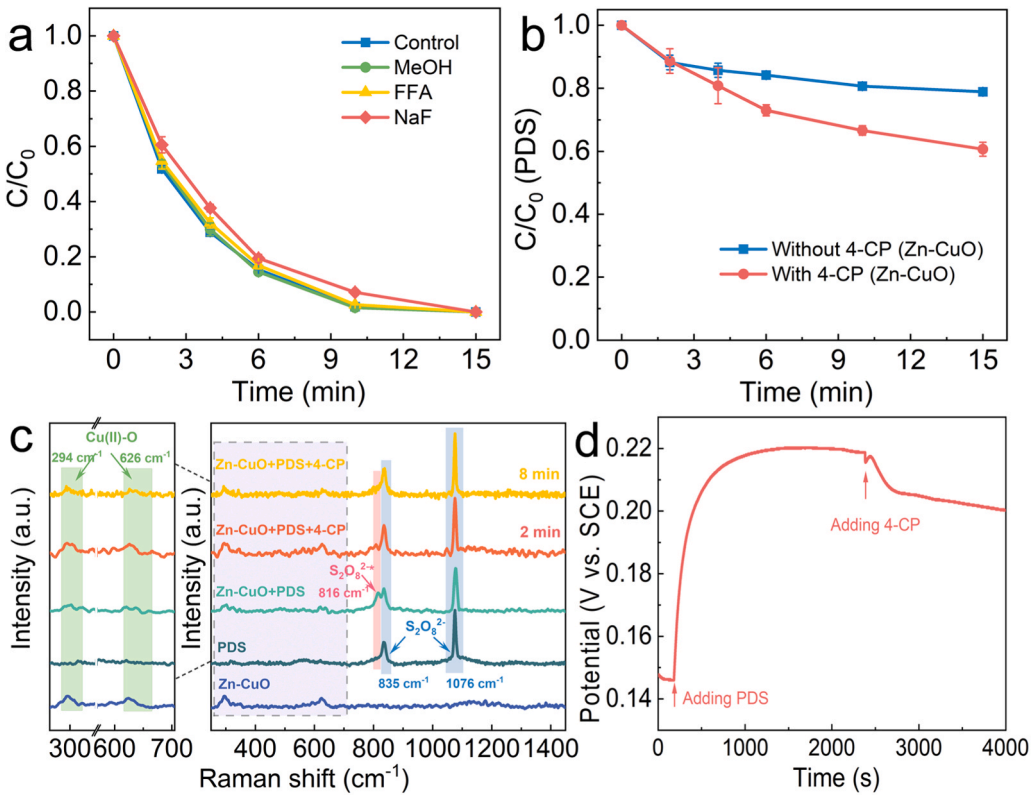

Fig. 3. (a) Lack of inhibition of 4-CP degradation by various quenchers added to the Zn-CuO/PDS system; (b) PDS decomposition with or without the presence of 4-CP in the Zn-CuO/PDS system; (c) In situ Raman spectra of the Zn-CuO/PDS system; (d) Open-circuit potential curves of the Zn-CuO/PDS system. Conditions: $[4\text{-CP}]_0$ = 10 mg/L (a, b and c) or 40 mg/L (d), [catalyst] = 0.2 g/L, [PDS] = 0.2 mM (a, b, and c) or 0.4 mM (d), [MeOH] = 200 mM, [FFA] = [NaF] = 2 mM, initial pH = 7.0.

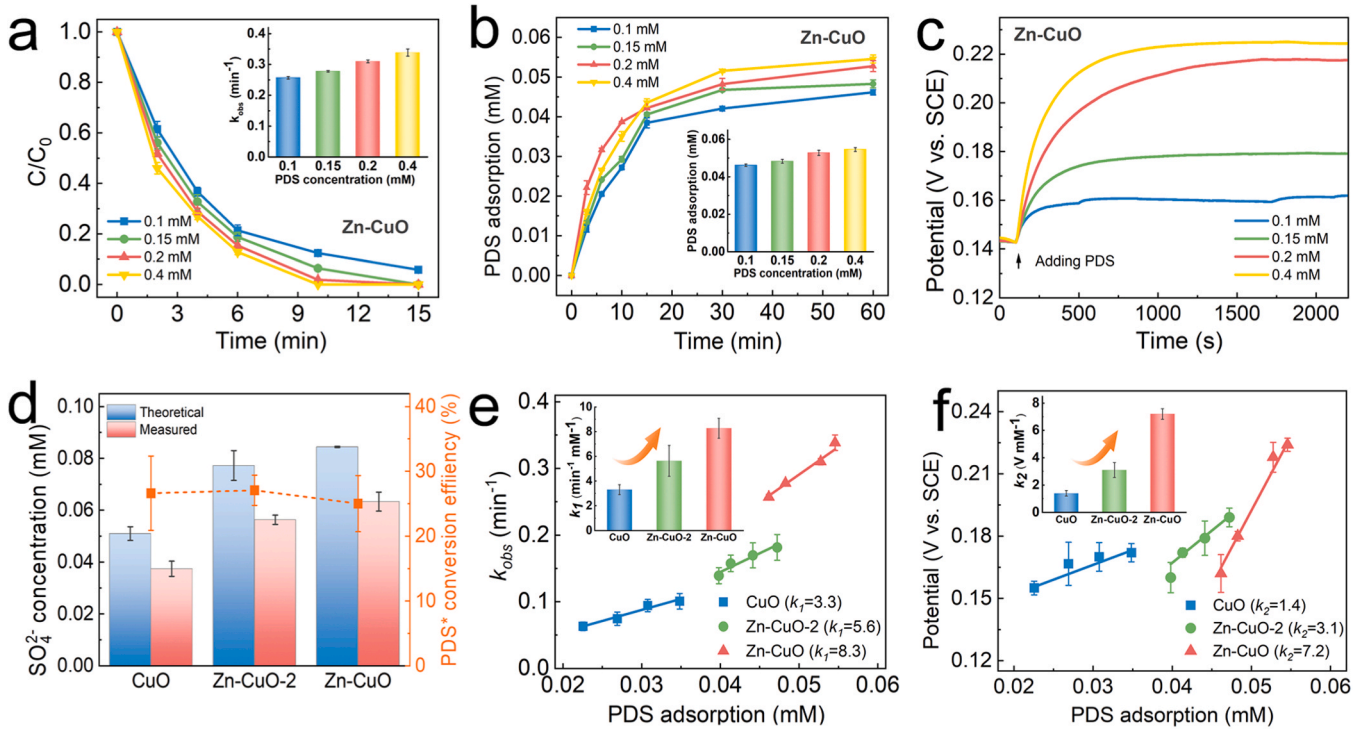

Fig. 4. (a) 4-CP degradation, (b) PDS adsorption, and (c) open-circuit potential for the Zn-CuO/PDS system with different initial PDS dosages; (d) Theoretical SO_4^{2-} concentration for complete PDS decomposition and measured SO_4^{2-} concentration, and corresponding PDS* conversion efficiency; Correlations between (e) k_{obs} and PDS adsorption quantity, (f) PDS adsorption quantity and potential of PDS*. Conditions: $[4\text{-CP}]_0$ = 10 mg/L, [catalyst] = 0.2 g/L, initial pH = 7.0.

3.4. Enhancement of PDS* generation and reactivity by Zn substitution

Notably, a similar "volcano-like" relationship was also observed between Zn contents and equilibrium PDS adsorption quantities (approximated by PDS adsorption quantity at 60 min) (Fig. S16a). The increased PDS adsorption can be partially attributed to changes in zeta potential resulting from Zn doping (Fig. S16b). Moreover, PDS adsorption by different catalysts demonstrates a linear relationship with k_{obs}, suggesting PDS adsorption is essential for PDS activation and subsequent 4-CP degradation (Fig. S16c).

To understand how enhanced PDS adsorption improves PDS activation, investigations into k_{obs}, the adsorption quantity of PDS, and the open circuit potential of surface-activated PDS* were carried out in CuO/PDS, Zn-CuO-2/PDS, and Zn-CuO/PDS systems. The 4-CP degradation rate constants increased from 0.26 to 0.34 min^{-1} as the initial PDS concentration rose from 0.1 to 0.4 mM (Fig. 4a). PDS adsorption conformed well to Langmuir isotherm (Figs. 4b and S17). Since the experimental PDS dosages were much lower than the fitted maximum PDS adsorption capacity (Q_{max}) for Zn-CuO, the equilibrium PDS adsorption mass (Q_e) increased with the initial PDS concentration. As a result, the potential of Zn-CuO/PDS* also increased with the PDS dosage (Fig. 4c). Similar trends were observed for CuO/PDS (Fig. S18) and Zn-CuO-2/PDS systems (Fig. S19). Note that the evaluation of PDS* generation cannot rely solely on PDS adsorption quantification since the conversion efficiency of adsorbed PDS into PDS* may vary. Thus, PDS* conversion efficiency, which represents the ratio of adsorbed PDS that is converted into reactive PDS*, was evaluated in different systems. The calculation of PDS* conversion efficiency involved determining the difference between the theoretically expected SO_4^{2-} concentration resulting from complete PDS decomposition and the actual SO_4^{2-} concentration (Text S4). Fig. 4d shows that CuO/PDS (27 ± 5.7%), Zn-CuO-2/PDS (27 ± 2.3%), and Zn-CuO/PDS (25 ± 4.3%) systems exhibited similar PDS* conversion efficiencies. Therefore, we postulate that Zn substitution enhances PDS adsorption but maintains similar PDS* conversion efficiencies, thereby facilitating PDS* generation. The improved PDS* generation is further supported by the impact of catalyst dosage. As shown in Figs. S20a-c, 4-CP degradation was enhanced with a higher catalyst dosage. To strike a balance between catalyst cost considerations and catalytic performance, the catalyst dosages for experiments were set at 0.2 g/L. The slope (r, min L g^{-1}) between k_{obs} and catalyst dosage exhibited an upward trend with increasing Zn contents, which can be ascribed to the improved efficiency of PDS adsorption and PDS* generation (Fig. S20d).

The quantity of PDS adsorption at different initial PDS concentrations shows a positive linear relationship with k_{obs} ($R^2 > 0.90$, $p < 0.05$, Fig. 4e). This slope (k_1, min^{-1} mM^{-1}) represents the increased oxidation rates per adsorbed PDS molecule, reflecting the apparent utilization efficiency of adsorbed PDS. Owing to the observed invariable PDS* conversion efficiency, k_1 also indicates the apparent utilization efficiency of PDS*, which may inherently depend on PDS* reactivity [26,32]. The k_1 value significantly increased from 3.3 ± 0.4 min^{-1} mM^{-1} for the CuO/PDS system to 8.3 ± 0.8 min^{-1} mM^{-1} for the Zn-CuO/PDS system, suggesting an enhanced apparent utilization efficiency of PDS* after Zn substitution. However, comparable slopes (s, min^{-1} V^{-1}) were observed between the open circuit potential of the catalyst with the adsorbed PDS molecules (PDS*) and k_{obs} in different systems (Fig. S21), suggesting that the electron transfer rates of catalysts were comparable [26].

The slope (k_2, V mM^{-1}) between the PDS adsorption quantity and the potential of PDS* was further assessed. Essentially, k_2 quantifies the increased PDS* potential upon adsorbing a specific amount of PDS. Thus, k_2 can be regarded as "PDS* reactivity", reflecting the intrinsic oxidation capacity of PDS* over catalysts. A well-fitted positive linear was observed in Fig. 4f ($R^2 > 0.91$, $p < 0.05$), with the slope following the order of Zn-CuO (7.2 ± 0.4 V mM^{-1}) > Zn-CuO-2 (3.1 ± 0.6 V mM^{-1}) > CuO (1.4 ± 0.2 V mM^{-1}), which was aligned with 4-CP degradation efficiency. The highest k_2 value observed in the Zn-CuO/PDS system indicates that, upon adsorbing a specific amount of PDS, Zn-CuO/PDS* attains the highest potential. Consequently, the increased apparent utilization efficiency of PDS* (k_1) resulting from Zn doping is essentially attributed to the augmented formation of complexes possessing superior reactivity (k_2).

Density functional theory (DFT) calculations were also conducted to understand the Zn-substitution-enhanced PDS* generation and reactivity. The adsorption energy of PDS on Zn-CuO (E_{ads} = −3.78 eV) is more negative than that on CuO (E_{ads} = −3.43 eV, Fig. 5a and Fig. S22), which is consistent with the experimental results that Zn substitution facilitates PDS adsorption (Fig. S16a). PDS adsorbed on Zn-CuO surface exhibits a longer O−O bond length (1.51 Å) than that on CuO surface, suggesting a stronger reactivity of the adsorbed PDS, as indicated by the higher k_2 value of the Zn-CuO/PDS system. The charge-density difference diagrams (Fig. S23) prove the occurrence of electron transfer from the catalysts to PDS, and the transferred Bader charge increases from 1.41 e to 1.46 e, indicating enhanced ability for directional electron transfer from Cu to PDS. Thus, all the above analyses support that Zn substitution contributed to the efficient production of PDS* with strong PDS* reactivity.

Upon PDS adsorption, only the d-band center of the spin-down electrons displays a noticeable shift (from −2.25 eV to −2.33 eV, Fig. S24), indicating that PDS adsorption is primarily governed by spin-down electrons [17]. Consequently, the d-band center of the spin-down electrons between CuO and Zn-CuO was compared through projected density of states (PDOS) calculations. Fig. 5c demonstrates that the d-band center of Zn-CuO (−2.25 eV) is closer to the Fermi level in comparison to that of CuO (−2.27 eV). This suggests that Zn substitution regulates the electron distribution of the Cu 3d orbital, and the less negative d-band center facilitates PDS adsorption, resulting in more negative adsorption energy, which is consistent with the above theoretical calculation results [49,64].

The Gibbs free energy of the reaction (Fig. 5d) indicates that both PDS adsorption (step (I) to (II)) and dissociation (step (II) to (III)) are exothermic processes. PDS adsorption onto Zn-CuO is more thermodynamically favorable than that of CuO. The dissociation energy of PDS on Zn-CuO (E_{dis} = −0.53 eV) is much smaller than that of CuO (E_{dis} = −0.85 eV), indicating that the O−O bond is more susceptible to breaking on the Zn-CuO surface [60]. The desorption of the second SO_4* to generate SO_4^{2-} (step (IV) to (V)) experiences the highest energy barrier, rendering it the rate-determining step for both Zn-CuO and CuO. The energy barrier decreases from 3.52 eV to 3.38 eV after Zn substitution. Therefore, Zn substitution simultaneously facilitates PDS adsorption and reduces the energy barrier for SO_4^{2-} desorption, contributing to enhanced PDS* generation and reactivity for 4-CP degradation.

4. Conclusions

In this work, we developed an approach to enhance reactive species (PDS*) generation and reactivity for efficient wastewater treatment. The substitution of earth-abundant Zn atoms into CuO lattice avoids the introduction of extra active sites, thus allowing us to discern the mechanisms for improved catalytic activity exhibited by Zn-CuO. The similar PDS* conversion efficiency reveals that PDS adsorption predominantly governs PDS* generation. Introducing the metric of "PDS* reactivity", represented as the slope between PDS* potential and PDS adsorption quantity, broadens the perspective on promoting PDS activation from merely increasing PDS adsorption to enhancing both PDS* generation and reactivity. Note that PDS* reactivity can be enhanced by modifying the d-band center of substrates through heteroatom substitution. The Cu-O-Zn coordination upshifts the d-band center of Cu sites, thus facilitating PDS adsorption and enhancing PDS* reactivity, and accordingly significantly improving the activity of Zn-CuO in Fenton-like reactions. Although certain limitations, such as

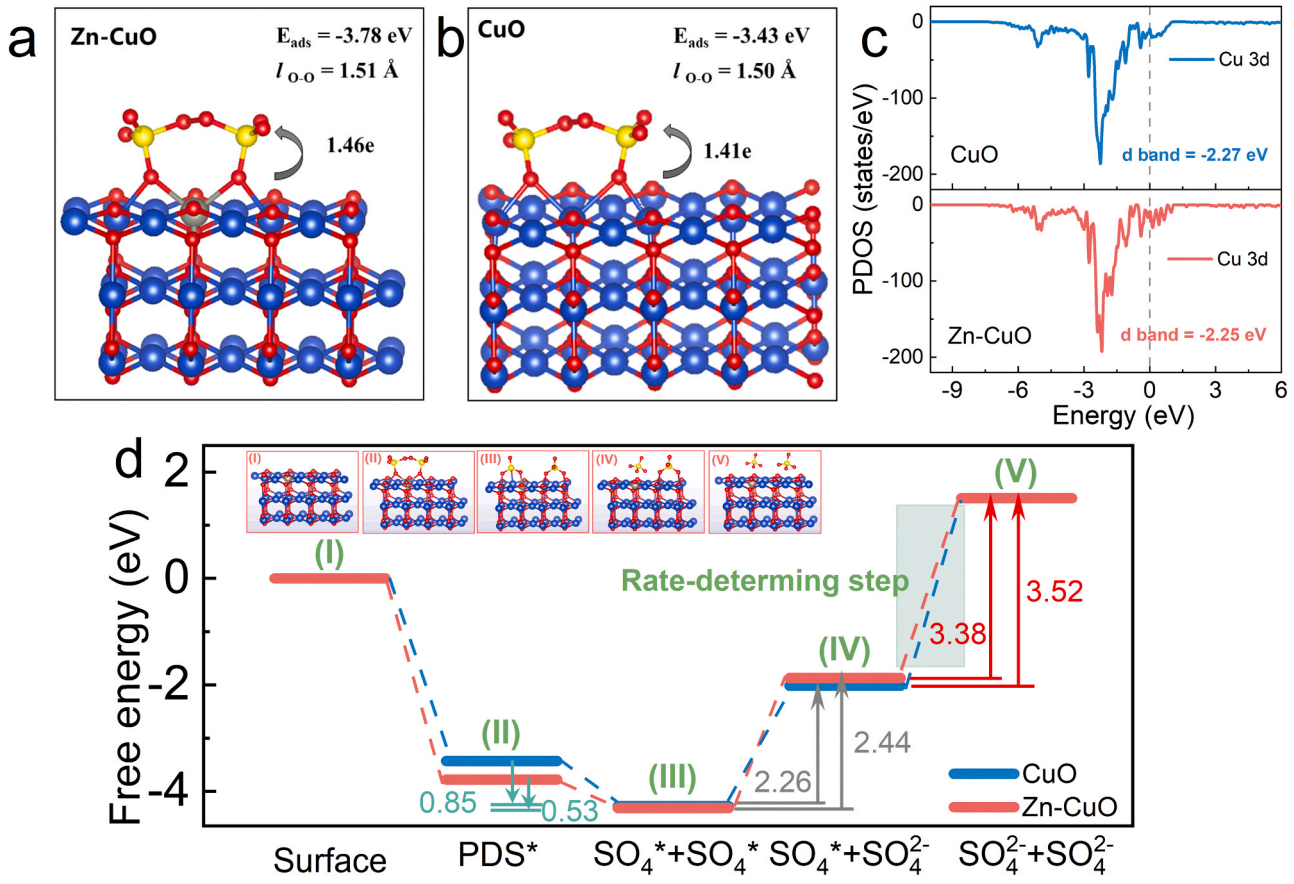

Fig. 5. DFT simulations showing adsorption of PDS on (a) Zn-CuO and (b) CuO; (c) PDOS of Cu 3d CuO and Zn-CuO; (d) Reaction path of and free energy profile of PDS activation.

means of improving PDS* conversion efficiency and the impact of various heteroatom substitutions necessitate further investigation, this work significantly advances mechanistic understanding of the intrinsic reactivity of reactive species in PDS-based AOPs, and introduces new possibilities for enhancing Fenton-like reactions by improving the reactivity of reactive species.

Environmental implication

Despite being relatively inexpensive, PDS is often underutilized in persulfate-based AOPs due to steric hindrance from its two SO_3 moieties, making it less reactive than PMS. This study addresses this limitation by simultaneously enhancing PDS* generation and reactivity, by incorporating earth-abundant Zn atoms into the CuO lattice. This modification upshifts the d-band center of Cu sites and optimizes the energy barrier for PDS activation. Consequently, the enhanced PDS* generation and reactivity result in superior 4-chlorophenol removal efficiency. This work opens an avenue for designing highly active catalysts by enhancing reactive species reactivity for efficient AOPs in water purification.

CRediT authorship contribution statement

Cui Jiahao: Formal analysis. **Lang Junyu:** Visualization, Validation. **Rao Qunli:** Resources, Formal analysis. **Zhou Baoxue:** Resources. **Long Mingce:** Writing – review & editing, Supervision, Resources, Funding acquisition, Conceptualization. **Alvarez Pedro J. J.:** Writing – review & editing, Funding acquisition. **Wei Yan:** Writing – original draft, Visualization, Validation, Methodology, Investigation, Formal analysis, Data curation. **Miao Jie:** Methodology, Funding acquisition, Formal analysis.

Declaration of Competing Interest

The authors declare that they have no known competing financial interests or personal relationships that could have appeared to influence the work reported in this paper.

Data availability

Data will be made available on request.

Acknowledgments

Financial supports from the National Natural Science Foundation of China (Nos. 22376138, 52070128, and 22106104), National Key R&D Program of China (2022YFA1205602) and NSF ERC on Nanotechnology-Enabled Water Treatment (EEC-1449500) are gratefully acknowledged.

Appendix A. Supporting information

Supplementary data associated with this article can be found in the online version at doi:10.1016/j.jhazmat.2024.133753.

References

[1] Aziz, K.H.H., Miessner, H., Mueller, S., Mahyar, A., Kalass, D., Moeller, D., Khorshid, I., Rashid, M.A.M., 2018. Comparative study on 2,4-dichlorophenoxyacetic acid and 2,4-dichlorophenol removal from aqueous solutions via ozonation, photocatalysis and non-thermal plasma using a planar falling film reactor. J Hazard Mater 343, 107–115. https://doi.org/10.1016/j.jhazmat.2017.09.025.

[2] Basera, P., Saini, S., Arora, E., Singh, A., Kumar, M., Bhattacharya, S., 2019. Stability of non-metal dopants to tune the photo-absorption of TiO_2 at realistic temperatures and oxygen partial pressures: A hybrid DFT study. Sci Rep 9, 11427. https://doi.org/10.1038/s41598-019-47710-7.

[3] Chen, C., Liu, L., Guo, J., Zhou, L., Lan, Y., 2019. Sulfur-doped copper-cobalt bimetallic oxides with abundant Cu(I): A novel peroxymonosulfate activator for chloramphenicol degradation. Chem Eng J 361, 1304–1316. https://doi.org/10.1016/j.cej.2018.12.156.

[4] Deng, Y., Handoko, A.D., Du, Y., Xi, S., Yeo, B.S., 2016. In situ Raman spectroscopy of copper and copper oxide surfaces during electrochemical oxygen evolution reaction: Identification of Cu^{III} oxides as catalytically active species. ACS Catal 6, 2473–2481. https://doi.org/10.1021/acscatal.6b00205.

[5] Eshed, M., Lellouche, J., Gedanken, A., Banin, E., 2014. A Zn-doped CuO nanocomposite shows enhanced antibiofilm and antibacterial activities against Streptococcus mutans compared to nanosized CuO. Adv Funct Mater 24, 1382–1390. https://doi.org/10.1002/adfm.201302425.

[6] Grant, S.B., Saphores, J.D., Feldman, D.L., Hamilton, A.J., Fletcher, T.D., Cook, P. L., Stewardson, M., Sanders, B.F., Levin, L.A., Ambrose, R.F., Deletic, A., Brown, R., Jiang, S.C., Rosso, D., Cooper, W.J., Marusic, I., 2012. Taking the "waste" out of "wastewater" for human water security and ecosystem sustainability. Science 337, 681–686. https://doi.org/10.1126/science.1216852.

[7] Guan, C., Jiang, J., Luo, C., Pang, S., Jiang, C., Ma, J., Jin, Y., Li, J., 2017. Transformation of iodide by carbon nanotube activated peroxydisulfate and formation of iodoorganic compounds in the presence of natural organic matter. Environ Sci Technol 51, 479–487. https://doi.org/10.1021/acs.est.6b04158.

[8] Guo, Z., Li, C., Gao, M., Han, X., Zhang, Y., Zhang, W., Li, W., 2020. Mn-O covalency governs the intrinsic activity of Co-Mn spinel oxides for boosted peroxymonosulfate activation. Angew Chem Int Ed 59, 2–9. https://doi.org/10.1002/anie.202010828.

[9] Guo, Z., Si, Y., Xia, W., Wang, F., Liu, H., Yang, C., et al., 2022. Electron delocalization triggers nonradical Fenton-like catalysis over spinel oxides. Proc Natl Acad Sci USA 119, e2201607119. https://doi.org/10.1073/pnas.2201607119.

[10] Ho, S.H., Chen, Y., Li, R., Zhang, C., Ge, Y., Cao, G., Ma, M., Duan, X., Wang, S., Ren, N., 2019. N-doped graphitic biochars from C-phycocyanin extracted *Spirulina* residue for catalytic persulfate activation toward nonradical disinfection and organic oxidation. Water Res 159, 77–86. https://doi.org/10.1016/j.watres.2019.05.008.

[11] Hodges, B.C., Cates, E.L., Kim, J.H., 2018. Challenges and prospects of advanced oxidation water treatment processes using catalytic nanomaterials. Nat Nanotechnol 13, 642–650. https://doi.org/10.1038/s41565-018-0216-x.

[12] Hu, P., Su, H., Chen, Z., Yu, C., Li, Q., Zhou, B., Alvarez, P.J.J., Long, M., 2017. Selective degradation of organic pollutants using an efficient metal-free catalyst derived from carbonized polypyrrole via peroxymonosulfate activation. Environ Sci Technol 51, 11288–11296. https://doi.org/10.1021/acs.est.7b03014.

[13] Jiang, Z., Tian, M., Jing, M., Chai, S., Jian, Y., Chen, C., Douthwaite, M., Zheng, L., Ma, M., Song, W., Liu, J., Yu, J., He, C., 2022. Modulating the electronic metal-support interactions in single-atom Pt_1-CuO catalyst for boosting acetone oxidation. Angew Chem Int Ed 61, e202200763. https://doi.org/10.1002/anie.202200763.

[14] Kau, L.S., Hodgson, K.O., Solomon, E.I., 1989. X-ray absorption edge and EXAFS study of the copper sites in zinc oxide methanol synthesis catalysts. J Am Chem Soc 111, 7103–7109. https://doi.org/10.1021/ja00200a032.

[15] Lee, H., Kim, H.I., Weon, S., Choi, W., Hwang, Y.S., Seo, J., Lee, C., Kim, J.H., 2016. Activation of persulfates by graphitized nanodiamonds for removal of organic compounds. Environ Sci Technol 50, 10134–10142. https://doi.org/10.1021/acs.est.6b02079.

[16] Lee, J., Von Gunten, U., Kim, J.H., 2020. Persulfate-based advanced oxidation: critical assessment of opportunities and roadblocks. Environ Sci Technol 54, 3064–3081. https://doi.org/10.1021/acs.est.9b07082.

[17] Li, F., Huang, J., Wang, J., Li, Q., 2019. Spin-Transport tuning of individual magnetic Mn-salophen molecule via chemical adsorption. Molecules 24, 1747. https://doi.org/10.3390/molecules24091747.

[18] Li, F., Lu, Z., Li, T., Zhang, P., Hu, C., 2022. Origin of the excellent activity and selectivity of a single-atom copper catalyst with unsaturated Cu-N_2 sites via peroxydisulfate activation: Cu(III) as a dominant oxidizing species. Environ Sci Technol 56, 8765–8775. https://doi.org/10.1021/acs.est.2c00369.

[19] Li, H., Shang, J., Yang, Z., Shen, W., Ai, Z., Zhang, L., 2017. Oxygen vacancy associated surface Fenton chemistry: surface structure dependent hydroxyl radicals generation and substrate dependent reactivity. Environ Sci Technol 51, 5685–5694. https://doi.org/10.1021/acs.est.7b00040.

[20] Liang, C., Huang, C., Mohanty, N., Kurakalva, R.M., 2008. A rapid spectrophotometric determination of persulfate anion in ISCO. Chemosphere 73, 1540–1543. https://doi.org/10.1016/j.chemosphere.2008.08.043.

[21] Liu, B., Li, Y., Wu, Y., Xing, S., 2021. Enhanced degradation of ofloxacin by persulfate activation with Mn doped CuO: Synergetic effect between adsorption and non-radical activation. Chem Eng J 417, 127972. https://doi.org/10.1016/j.cej.2020.127972.

[22] Lu, Y., Jiang, X., Wu, C., Lin, L., Huang, Z., Lin, Z., Humphrey, M.G., Zhang, C., 2021. Molecular engineering toward an enlarged optical band gap in a bismuth sulfate via homovalent cation substitution. Inorg Chem 60, 5851–5859. https://doi.org/10.1021/acs.inorgchem.1c00269.

[23] Luo, H., Wan, Y., Zhou, H., Cai, Y., Zhu, M., Dang, Z., Yin, H., 2022. Mechanisms and influencing factors for electron transfer complex in metal-biochar nanocomposites activated peroxydisulfate. J Hazard Mater 438, 129461. https://doi.org/10.1016/j.jhazmat.2022.129461.

[24] Ma, Y., Wang, D., Xu, Y., Lin, H., Zhang, H., 2022. Nonradical electron transfer-based peroxydisulfate activation by a Mn-Fe bimetallic oxide derived from spent alkaline battery for the oxidation of bisphenol A. J Hazard Mater 436, 129172. https://doi.org/10.1016/j.jhazmat.2022.129172.

[25] Miao, J., Geng, W., Alvarez, P.J.J., Long, M., 2020. 2D N-doped porous carbon derived from polydopamine-coated graphitic carbon nitride for efficient nonradical activation of peroxymonosulfate. Environ Sci Technol 54, 8473–8481. https://doi.org/10.1021/acs.est.0c03207.

[26] Miao, J., Zhu, Y., Lang, J., Zhang, J., Cheng, S., Zhou, B., Zhang, L., Alvarez, P.J.J., Long, M., 2021. Spin-state-dependent peroxymonosulfate activation of single-atom M–N moieties via a radical-free pathway. ACS Catal 11, 9569–9577. https://doi.org/10.1021/acscatal.1c02031.

[27] Mustafa, F.S., Aziz, K.H.H., 2023. Heterogeneous catalytic activation of persulfate for the removal of rhodamine B and diclofenac pollutants from water using iron-impregnated biochar derived from the waste of black seed pomace. Process Saf Environ 170, 436–448. https://doi.org/10.1016/j.psep.2022.12.030.

[28] Niu, B., Wang, L., Li, M., Yao, W., Zang, K., Zhou, L., Hu, X., Zheng, Y., 2022. Lattice B-doping evolved ferromagnetic perovskite-like catalyst for enhancing persulfate-based degradation of norfloxacin. J Hazard Mater 425, 127949. https://doi.org/10.1016/j.jhazmat.2021.127949.

[29] Oh, W.D., Wong, Z., Chen, X., Lin, K.Y.A., Veksha, A., Lisak, G., He, C., Lim, T.T., 2020. Enhanced activation of peroxydisulfate by CuO decorated on hexagonal boron nitride for bisphenol A removal. Chem Eng J 393, 124714. https://doi.org/10.1016/j.cej.2020.124714.

[30] Ren, D., Gao, J., Pan, L., Wang, Z., Luo, J., Zakeeruddin, S.M., Hagfeldt, A., Grätzel, M., 2019. Atomic layer deposition of ZnO on CuO enables selective and efficient electroreduction of carbon dioxide to liquid fuels. Angew Chem Int Ed 58, 15036–15040. https://doi.org/10.1002/anie.201909610.

[31] Ren, W., Cheng, C., Shao, P., Luo, X., Zhang, H., Wang, S., Duan, X., 2022. Origins of electron-transfer regime in persulfate-based nonradical oxidation processes. Environ Sci Technol 56, 78–97. https://doi.org/10.1021/acs.est.1c05374.

[32] Ren, W., Nie, G., Zhou, P., Zhang, H., Duan, X., Wang, S., 2020. The intrinsic nature of persulfate activation and N-doping in carbocatalysis. Environ Sci Technol 54, 6438–6447. https://doi.org/10.1021/acs.est.0c01161.

[33] Ren, W., Xiong, L., Nie, G., Zhang, H., Duan, X., Wang, S., 2020. Insights into the electron-transfer regime of peroxydisulfate activation on carbon nanotubes: the role of oxygen functional groups. Environ Sci Technol 54, 1267–1275. https://doi.org/10.1021/acs.est.9b06208.

[34] Schwarzenbach, R.P., Escher, B.I., Fenner, K., Hofstetter, T.B., Johnson, C.A., Von Gunten, U., Wehrli, B., 2006. The challenge of micropollutants in aquatic systems. Science 313, 1072–1077. https://doi.org/10.1126/science.1127291.

[35] Shi, Q., Ji, Y., Chen, W., Zhu, Y., Li, J., Liu, H., Li, Z., Tian, S., Wang, L., Zhong, Z., Wang, L., Ma, J., Li, Y., Su, F., 2020. Single-atom Sn-Zn pairs in CuO catalyst promote dimethyldichlorosilane synthesis. Natl Sci Rev 7, 600–608. https://doi.org/10.1093/nsr/nwz196.

[36] Song, C., Zhan, Q., Liu, F., Wang, C., Li, H., Wang, X., Guo, X., Cheng, Y., Sun, W., Wang, L., Qian, J., Pan, B., 2022. Overturned loading of inert CeO_2 to active Co_3O_4 for unusually improved catalytic activity in Fenton-like reactions. Angew Chem Int Ed 61, e202200406. https://doi.org/10.1002/anie.202200406.

[37] Speight, J.G., 2005. Lange's Handbook of Chemistry. McGRAW-HILL.

[38] Su, H., Wei, Y., Qu, X., Yu, C., Li, Q., Alvarez, P.J.J., Long, M., 2020. Mechanistic inference on the reaction kinetics of phenols and anilines in carbon nanotubes-activated peroxydisulfate systems: pp-LFERs and QSARs analyses. Chem Eng J 385, 123923. https://doi.org/10.1016/j.cej.2019.123923.

[39] Sun, X., Sun, L., Li, G., Tuo, Y., Ye, C., Yang, J., Low, J., Yu, X., Bitter, J.H., Lei, Y., Wang, D., Li, Y., 2022. Phosphorus tailors the d-band center of copper atomic sites for efficient CO_2 photoreduction under visible-light irradiation. Angew Chem Int Ed 61, e202207677. https://doi.org/10.1002/anie.202207677.

[40] Tang, M., Wan, J., Wang, Y., Ye, G., Yan, Z., Ma, Y., Sun, J., 2023. Insights into molecular imprinting polydopamine in-situ activating peroxydisulfate for targeted removal of refractory organic pollutants: Overlooked N site. Appl Catal B: Environ 334, 122852. https://doi.org/10.1016/j.apcatb.2023.122852.

[41] Tang, Z., Zhao, P., Wang, H., Liu, Y., Bu, W., 2021. Biomedicine meets Fenton chemistry. Chem Rev 121, 1981–2019. https://doi.org/10.1021/acs.chemrev.0c00977.

[42] Tong, M., Sun, F., Xie, Y., Wang, Y., Yang, Y., Tian, C., Wang, L., Fu, H., 2021. Operando cooperated catalytic mechanism of atomically dispersed Cu-N_4 and Zn-N_4 for promoting oxygen reduction reaction. Angew Chem Int Ed 60, 14005–14012. https://doi.org/10.1002/anie.202102053.

[43] Wang, B., Cheng, C., Jin, M., He, J., Zhang, H., Ren, W., Li, J., Wang, D., Li, Y., 2022. A site distance effect induced by reactant molecule matchup in single-atom catalysts for Fenton-like reactions. Angew Chem Int Ed 61, e202207268. https://doi.org/10.1002/anie.202207268.

[44] Wang, M., Liu, L., Wen, J., Ding, Y., Xi, J., Li, J., Lu, F., Wang, W., Xu, J., 2022. Multimetallic CuCoNi oxide nanowires in situ grown on a nickel foam substrate catalyze persulfate activation via mediating electron transfer. Environ Sci Technol 56, 12613–12624. https://doi.org/10.1021/acs.est.2c04312.

[45] Wei, Y., Miao, J., Ge, J., Lang, J., Yu, C., Zhang, L., Alvarez, P.J.J., Long, M., 2022. Ultrahigh peroxymonosulfate utilization efficiency over CuO nanosheets via heterogeneous Cu(III) formation and preferential electron transfer during degradation of phenols. Environ Sci Technol 56, 8984–8992. https://doi.org/10.1021/acs.est.2c01968.

[46] Wei, Y., Su, H., Zhang, Y., Zheng, L., Pan, Y., Su, C., Geng, W., Long, M., 2019. Efficient peroxodisulfate activation by iodine vacancy rich bismuth oxyiodide: A vacancy induced mechanism. Chem Eng J 375, 121971. https://doi.org/10.1016/j.cej.2019.121971.

[47] Wu, B., Li, Z., Zu, Y., Lai, B., Wang, A., 2023. Polar electric field-modulated peroxymonosulfate selective activation for removal of organic contaminants via non-radical electron transfer process. Water Res 246, 120678. https://doi.org/10.1016/j.watres.2023.120678.

[48] Wu, L., Wu, T., Liu, Z., Tang, W., Xiao, S., Shao, B., Liang, Q., He, Q., Pan, Y., Zhao, C., Liu, Y., Tong, S., 2022. Carbon nanotube-based materials for persulfate activation to degrade organic contaminants: Properties, mechanisms and modification insights. J Hazard Mater 431, 128536. https://doi.org/10.1016/j.jhazmat.2022.128536.

[49] Wu, Q., Yang, Z., Wang, Z., Wang, W., 2023. Oxygen doping of cobalt-single-atom coordination enhances peroxymonosulfate activation and high-valent cobalt-oxo species formation. Proc Natl Acad Sci USA 120, e2219923120. https://doi.org/10.1073/pnas.2219923120.

[50] Xie, L., Wang, P., Li, Y., Zhang, D., Shang, D., Zheng, W., Xia, Y., Zhan, S., Hu, W., 2022. Pauling-type adsorption of O_2 induced electrocatalytic singlet oxygen production on N-CuO for organic pollutants degradation. Nat Commun 13, 5560. https://doi.org/10.1038/s41467-022-33149-4.

[51] Xie, M., Dai, F., Li, J., Dang, X., Guo, J., Lv, W., Zhang, Z., Lu, X., 2021. Tailoring the electronic metal-support interactions in supported atomically dispersed gold catalysts for efficient Fenton-like reaction. Angew Chem Int Ed 60, 14491–14496. https://doi.org/10.1002/anie.202103652.

[52] Xu, J., Ji, W., Shen, Z., Li, W., Tang, S., Ye, X., Jia, D., Xin, X., 1999. Raman spectra of CuO nanocrystals. J Raman Spectrosc 30, 413–415. https://doi.org/10.1002/(SICI)1097-4555(199905)30:5<413::AID-JRS387>3.0.CO;2-N.

[53] Yang, M., Hou, Z., Zhang, X., Gao, B., Li, Y., Shang, Y., Yue, Q., Duan, X., Xu, X., 2022. Unveiling the origins of selective oxidation in single-atom catalysis via Co-N_4-C intensified radical and nonradical pathways. Environ Sci Technol 56, 11635–11645. https://doi.org/10.1021/acs.est.2c01261.

[54] Yun, E.T., Moon, G.H., Lee, H., Jeon, T.H., Lee, C., Choi, W., Lee, J., 2018. Oxidation of organic pollutants by peroxymonosulfate activated with low-temperature-modified nanodiamonds: Understanding the reaction kinetics and mechanism. Appl Catal B: Environ 237, 432–441. https://doi.org/10.1016/j.apcatb.2018.04.067.

[55] Zhang, H., An, Q., Su, Y., Quan, X., Chen, S., 2023. Co_3O_4 with upshifted d-band center and enlarged specific surface area by single-atom Zr doping for enhanced PMS activation. J Hazard Mater 448, 130987. https://doi.org/10.1016/j.jhazmat.2023.130987.

[56] Zhang, K., Kim, D., Hu, Z., Park, M., Noh, G., Yang, Y., Zhang, J., Lau, V.W., Chou, S.L., Cho, M., Choi, S.Y., Kang, Y.M., 2019. Manganese based layered oxides with modulated electronic and thermodynamic properties for sodium ion batteries. Nat Commun 10, 5203. https://doi.org/10.1038/s41467-018-07646-4.

[57] Zhang, T., Chen, Y., Wang, Y.R., Le Roux, J., Yang, Y., Croue, J.P., 2014. Efficient peroxydisulfate activation process not relying on sulfate radical generation for water pollutant degradation. Environ Sci Technol 48, 5868–5875. https://doi.org/10.1021/es501218f.

[58] Zhang, Y., Huang, G., Winter, L.R., Chen, J., Tian, L., Mei, S., Zhang, Z., Chen, F., Guo, Z., Ji, R., You, Y., Li, W., Liu, X., Yu, H., Elimelech, M., 2022. Simultaneous nanocatalytic surface activation of pollutants and oxidants for highly efficient water decontamination. Nat Commun 13, 3005. https://doi.org/10.1038/s41467-022-30560-9.

[59] Zhao, Y., Yu, L., Song, C., Chen, Z., Meng, F., Song, M., 2022. Selective degradation of electron-rich organic pollutants induced by CuO@biochar: the key role of outer-sphere interaction and singlet oxygen. Environ Sci Technol 56, 10710–10720. https://doi.org/10.1021/acs.est.2c01759.

[60] Zhao, Z., Wang, P., Song, C., Zhang, T., Zhan, S., Li, Y., 2023. Enhanced interfacial electron transfer by asymmetric Cu-O_V-In sites on In_2O_3 for efficient peroxymonosulfate activation. Angew Chem Int Ed, e202216403. https://doi.org/10.1002/anie.202216403.

[61] Zhi, J., Zhou, M., Zhang, Z., Reiser, O., Huang, F., 2021. Interstitial boron-doped mesoporous semiconductor oxides for ultratransparent energy storage. Nat Commun 12, 445. https://doi.org/10.1038/s41467-020-20352-4.

[62] Zhou, L., Li, P., Yang, X., Wu, J., Hou, B., Xu, B., Liu, X., Zhang, K., Jiang, W., 2023. Activated peroxymonosulfate with co-doped copper oxide nanomaterials for highly efficient degradation of organic pollutants. Sep Purif Technol 325, 124671. https://doi.org/10.1016/j.seppur.2023.124671.

[63] Zhou, Q., Song, C., Wang, P., Zhao, Z., Li, Y., Zhan, S., 2023. Generating dual-active species by triple-atom sites through peroxymonosulfate activation for treating micropollutants in complex water. Proc Natl Acad Sci USA 120, e2300085120. https://doi.org/10.1073/pnas.2300085120.

[64] Zhou, X., Ke, M., Huang, G., Chen, C., Chen, W., Liang, K., et al., 2022. Identification of Fenton-like active Cu sites by heteroatom modulation of electronic density. Proc Natl Acad Sci USA 119, e2119492119. https://doi.org/10.1073/pnas.2119492119.

[65] Zhou, X., Luo, M., Xie, C., Wang, H., Wang, J., Chen, Z., Xiao, J., Chen, Z., 2021. Tunable S doping from Co_3O_4 to Co_9S_8 for peroxymonosulfate activation: Distinguished radical/nonradical species and generation pathways. Appl Catal B: Environ 282, 119605. https://doi.org/10.1016/j.apcatb.2020.119605.